

# Orientation Dependent Directed Etching of Aluminum

Dong Nyung Lee<sup>†</sup> and Jong Hyun Seo<sup>1</sup>

*School of Materials Science and Engineering, Seoul National University, Seoul 151-744,  
Korea and Graduate Institute of Ferrous Technology,*

*Pohang University of Science and Technology, Pohang 790-784, Korea*

<sup>1</sup>*Department of Materials Science & Engineering, Hankuk Aviation University, Goyang-si 412-791, Korea  
(Received April 4, 2007; No Revision; Accepted June 4, 2009)*

The direct-current electroetching of high purity aluminum in hot aqueous-chloride solution produces a high density of micrometer-wide tunnels whose walls are made up of the {100} planes and penetrate aluminum in the <100> directions at rates of micrometer per second. In the process of the alternating-current pitting of aluminum, cathodic polarization plays an important role in the nucleation and growth of the pits during the subsequent polarization. The direct-current tunnel etching and alternating-current etching of aluminum are basically related to the formation of poorly crystallized or amorphous passive films. If the passive film forms on the wall, a natural misfit exists between the film and the aluminum substrate, which in turn gives rise to stress in both the film and the substrate. Even though the amorphous films do not have directed properties, their stresses are influenced by the substrate orientation. The films on elastically soft substrate are likely to be less stressed and more stable than those on elastically hard substrate. The hardest and softest planes of aluminum are the {111} and {100} planes, respectively. Therefore, the films on the {111} substrates are most likely to be attacked, and those on the {100} substrates are least likely to be attacked. For the tunnel etching, it follows that the tunnel walls tend to consist of the {100} planes. Meanwhile, the tunnel tip, where active corrosion takes place, tend to be made of four closely packed {111} planes in order to minimize the surface energy, which gives rise to the <100> tunnel etching.

**Keywords :** *aluminum, directed etching, direct-current electroetching, direct-current tunnel etching, alternating-current pitting*

## 1. Introduction

Electrochemical etching of aluminum has long been studied from the technical and scientific viewpoints. Etching of high purity aluminum foils for electrodes of aluminum capacitors is widely carried out to increase the surface area of the aluminum electrodes. In order to increase the specific area, or the real area per unit apparent area, we have to control pit nucleation and growth and tunnel etching. In order to control the technically important processes, we need scientific understanding of the aluminum-etching phenomena. One of unique phenomena in etching of aluminum is directed etching. In other words, etching is taking place in crystallographic directions of aluminum. This has motivated studies of the directed etching of aluminum.

A model for the directed etching has been suggested by Jeong et al.<sup>1)</sup> and Seo et al.,<sup>2)</sup> in which the stability or strain energy of amorphous aluminum oxide film is as-

sociated with the strain energy of the substrate. In this paper, the model is elaborated and various experimental results are explained by the model.

## 2. Substrate-orientation dependent stability of passive film

Aluminum is easily covered by oxides formed in air or even in etching atmosphere. The oxides are mostly amorphous and partially crystalline. Therefore, their chemical and mechanical properties are deemed to be isotropic. In order for aluminum covered with oxide or passive films to be attacked, the films have to be damaged first. Since the properties of films are isotropic, their damage is expected to be isotropic and in turn the aluminum substrate is expected to show isotropic etching or corrosion behavior. Contrary to the expectation, aluminum often show directed etching behavior. In this section, our earlier model for the directed etching behavior is elaborated, in which anisotropic elastic behavior of the aluminum substrate can influence the damage of the surface film.

<sup>†</sup> Corresponding author: dnlee@snu.ac.kr

We are concerned about oxide films which are associated with etching. They may be naturally formed oxides on the aluminum surface or passive oxide films formed on the aluminum surface during etching. Stresses can develop in the film resulting from elastic accommodation between the film and the substrate. Several investigators have reported that the anodic aluminum oxide film on aluminum is usually in a state of compressive stress, resulting from oxygen transport during film growth.<sup>3,4</sup> The compressive stress in the passive film induces the tensile stress in its underlying layer of substrate, and the tensile stress in the film induces the compressive stress in its underlying layer.

Fig. 1 shows how the compressive stress can be made in the film. A stress-free film attached on curved stress-free foil that is the same material as the substrate (substrate-f) is flattened against and bonded to the substrate. In this way, compressive stresses develop in the film, while tensile stresses develop in the substrate. Since there is no stress in the edge, the peak-stress in the film can vary along the film plane as shown in Fig. 2. For a film forming progressively along the substrate surface, the peak-stress profile in the film increases with increasing area of film as shown in Fig. 3 (a). When the peak stress

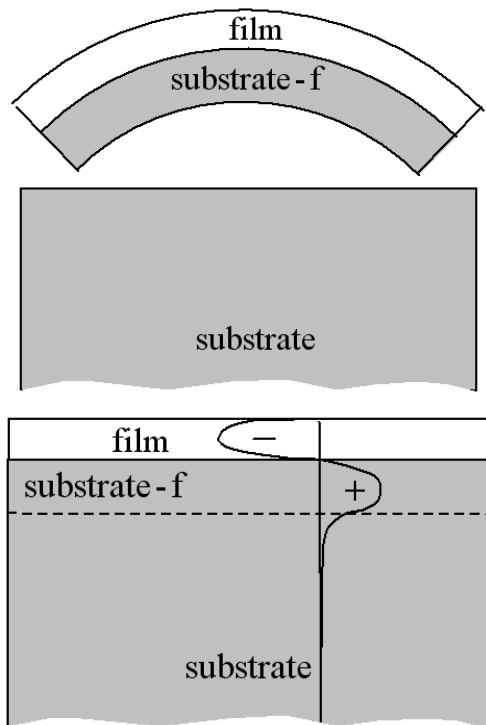


Fig. 1. Stress-free film attached on curved stress-free substrate foil (substrate-f) is flattened against and bonded to substrate to develop compressive stress (-) in film and tensile stress (+) in substrate underneath film.

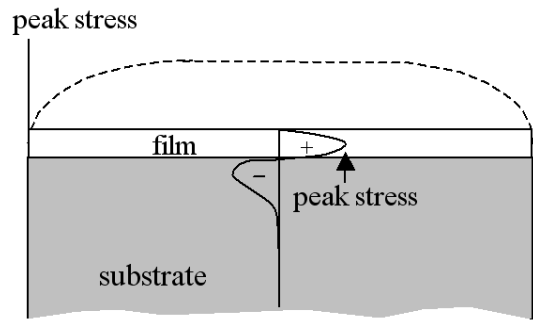
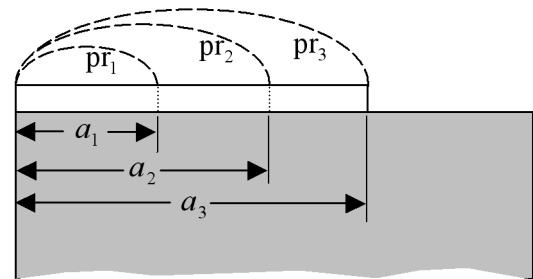
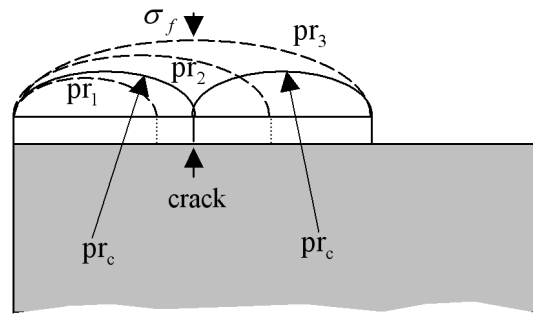


Fig. 2. Peak-stress profile in film.



(a)



(b)

Fig. 3. (a) Peak-stress profiles in film  $pr_i$  in film areas  $a_i$ . (b) When peak stress reaches fracture stress of film  $\sigma_f$ , film cracks, resulting in stress relaxation, and new peak-stress profiles  $pr_c$  are established.

in film reaches the fracture stress of the film, the film cracks and the stress relaxation occurs in the film as shown in Fig. 3 (b).

The stress and strain states of film can be approximated by the plane stress-equibiaxial strain state, because its thickness is negligibly small compared with the substrate thickness. Likewise, the substrate underneath the film is approximately in the plane stress-equibiaxial strain state. If the substrate is elastically unisotropic, the film behaves anisotropically, even though the film itself is isotropic. For example, the film on an elastically hard substrate is likely to have higher stresses or higher strain energy than that on an elastically soft substrate because the soft one can

be easily deformed to release the film stresses.

The plane stress-equibiaxial strain states ( $\sigma'_{33} = \sigma'_{23} = \sigma'_{13} = \sigma'_{12} = 0$ ,  $\varepsilon'_{11} = \varepsilon'_{22} = \varepsilon$ ), where  $\sigma$  and  $\varepsilon$  indicate stress and strain, respectively, and the subscripts 1 and 2 with prime indicate two arbitrary, mutually perpendicular axis directions on the surface and 3 the normal direction.

For the plane stress-equibiaxial strain states, the strain energy per unit volume of a crystal strained along the  $(hkl)$  plane is given by the following equation<sup>5)</sup>

$$w = \frac{\varepsilon^2}{2} \frac{S'_{11} + S'_{22} - 2S'_{12}}{S'_{11}S'_{22} - (S'_{12})^2} = \varepsilon^2 M \quad (1)$$

where  $M$  is equivalent to Young's modulus in the uniaxial stress state and may be called the biaxial elastic modulus in plane stress-equibiaxial strain state. The modulus  $M$  can function as a measure of the strain energy for the plane stress-equibiaxial strain state as Young's modulus  $E$  functions as a measure of the strain energy for the uniaxial stress state ( $w = E\varepsilon^2/2$ ). The compliances  $S'_{11}$ ,  $S'_{12}$ , and  $S'_{22}$  for cubic crystal are obtained by the tensor transformation as follows:

$$S'_{11} = S_{11} + [S_{44} - 2(S_{11} - S_{12})] (a_{11}^2 a_{12}^2 + a_{12}^2 a_{13}^2 + a_{13}^2 a_{11}^2) \quad (2)$$

$$S'_{12} = S_{12} + (S_{11} - S_{12} - S_{44}/2) (a_{11}^2 a_{21}^2 + a_{12}^2 a_{22}^2 + a_{13}^2 a_{23}^2) \quad (3)$$

$$S'_{22} = S_{11} + [S_{44} - 2(S_{11} - S_{12})] (a_{22}^2 a_{21}^2 + a_{21}^2 a_{23}^2 + a_{23}^2 a_{22}^2) \quad (4)$$

with

$$a_{ij} = \begin{bmatrix} \frac{-k}{\sqrt{h^2+k^2}} & \frac{h}{\sqrt{h^2+k^2}} & 0 \\ \frac{-hl}{\sqrt{h^2+k^2}\sqrt{h^2+k^2+l^2}} & \frac{-kl}{\sqrt{h^2+k^2}\sqrt{h^2+k^2+l^2}} & \frac{h^2+k^2}{\sqrt{h^2+k^2}\sqrt{h^2+k^2+l^2}} \\ \frac{h}{\sqrt{h^2+k^2+l^2}} & \frac{k}{\sqrt{h^2+k^2+l^2}} & \frac{l}{\sqrt{h^2+k^2+l^2}} \end{bmatrix} \quad (5)$$

where  $S_{ij}$  is the compliances referred to the symmetric axes.

For aluminum at 293 K,  $S_{11} = 0.01572$ ,  $S_{12} = -0.00583$ , and  $S_{44} = 0.03593 \text{ GPa}^{-1}$ .<sup>4)</sup> The  $M$  values for the  $\{001\}$ ,  $\{110\}$ , and  $\{111\}$  planes of aluminum are calculated to be 101, 104.7, and 114.9 GPa, respectively. In fact, the  $M$  values for the  $\{111\}$  and  $\{100\}$  planes are the highest and the lowest, respectively, as shown in Fig. 4. Therefore, the oxide films formed on the  $\{111\}$  and  $\{100\}$  orientated aluminum surfaces are likely to have the highest and lowest strain energies, respectively, and hence are likely to be attacked most and least in corrosion atmosphere, respectively. It is also noted that the difference in  $M$  be-

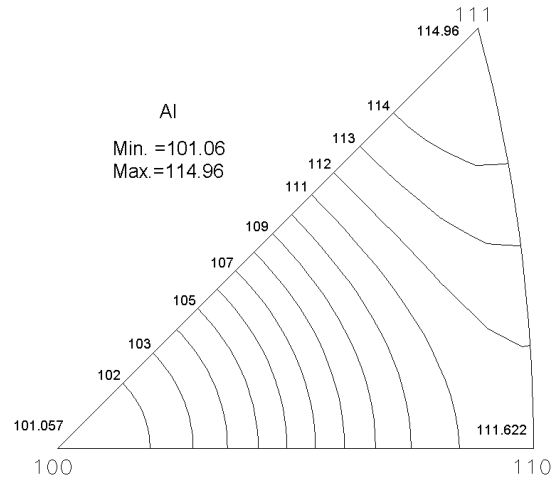


Fig. 4.  $M$  value of Al at room temperature.

tween the  $\{100\}$  and  $\{110\}$  planes is 3.7 GPa and that between the  $\{110\}$  and  $\{111\}$  planes is 10.2 GPa.

### 3. Pitting results and discussion

#### 3.1 Pit morphology

Fig. 5 shows the pit morphologies observed in the pitting experiments of 99.999% Al single crystal in 1 M HCl solution at 30 °C. The pits show crystallographic characteristics. The pit faces are made up of the  $\{100\}$  surfaces. Prior cathodic polarization has a significant influence on pit distribution. The shape of the aluminum etch pits resulting from ac etching is better delineated than that resulting from dc etching. When the aluminum specimen is etched by pulsed dc, the pit distribution is severely localized, and the sides of the gross pits are composed of sharply defined facets and steps, whereas these characteristics are virtually absent in the etch pits formed by ac square waveform. On the other hand, the distribution of the pits generated by ac is uniform on all the low index surfaces and the pit shape is regular.

In the growth of a crystal, the rapidly growing faces disappear, leaving the crystal bounded by the faces of slowest growth. These slow growing faces are usually the close packed crystal planes. Likewise, it is likely that the rapidly dissolving faces disappear first in pitting. Therefore, the shape of the etch pits is likely to be made of the most slowly dissolving faces during etching.

Fig. 6 shows transients of open circuit potential (OCP) for the  $\{111\}$ ,  $\{110\}$ , and  $\{100\}$  surfaces of aluminum single crystals in 1 M HCl solution. The initial decrease in the transients can be ascribed to the bare aluminum surface being exposed to the electrolyte, while the sub-

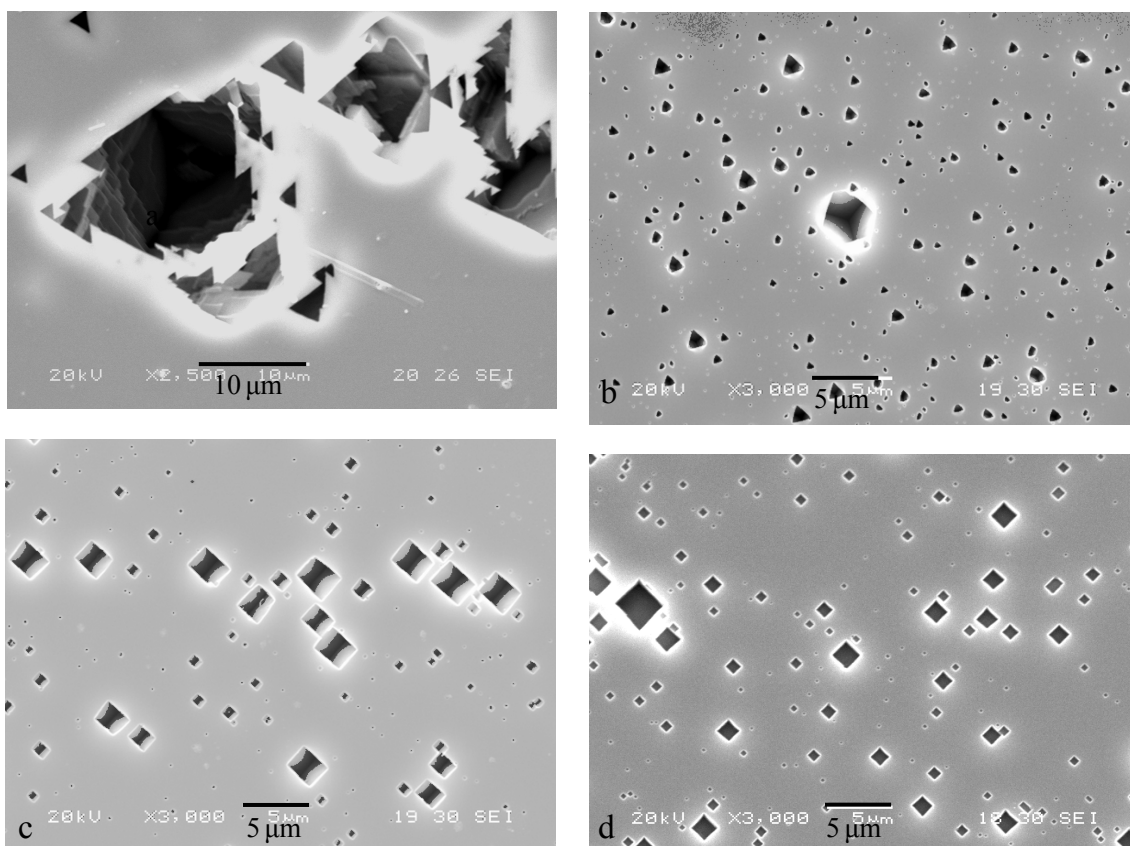


**Fig. 5.** SEM micrographs of Al surfaces pitted in 1 M HCl solution. (a) {111} surface pitted by pulsed dc waveform, (b) {111} surface pitted by ac waveform, (c) {110} surface pitted by ac waveform, (d) {100} surface pitted by ac waveform. (dc waveform:  $-0.5$  V/SCE for 100 ms; ac waveform:  $-2$  V/SCE for 100ms,  $-0.5$  V/SCE for 100ms).<sup>2)</sup>

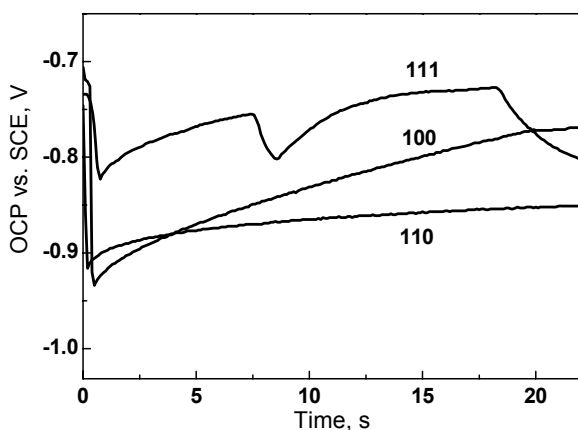


**Fig. 6.** Transients of open circuit potentials for {100}, {110}, and {111} surfaces of Al single crystal in 1 M solution<sup>2)</sup>

sequent increase in the transients is closely related to the repassivation of the bare aluminum surface. The slopes in the rising OCP curves for the {111} and {100} surfaces are higher than that of the {110} surface. This indicates

that the rate of formation of passive film on the exposed metal surface is the slowest on the {110} oriented surface. The saw-like transient curve for the {111} surface indicates that the repassivation film on the {111} surface seems to be easily broken by chloride ions, in comparison with the film on the {100} surface. This ready breakdown of the repassivation film can be ascribed to the higher elastic strain energy of the oxide film on the {111} surface of the aluminum crystal. This is consistent with our prediction concerning the stability of the oxide films depending on their substrate orientations (Section 2). The repassivation film, which is quickly formed on the {100} surface, is very stable and prevents the aluminum surface from further dissolving during the pits' growth. It results in the crystallographic etch pits being bounded by the {100} surfaces.

Figs. 7 and 8 shows observed etch pits and schematically drawn pits on the {110} and {111} surfaces, respectively. It can be seen that most etch pits are bounded by the {100} planes, on which the repassivated film is the most stable. Occasionally etch pits bounded by the {100},

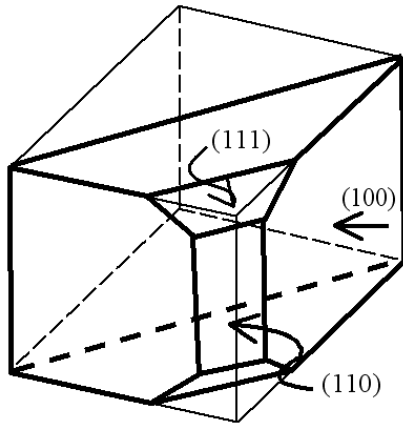
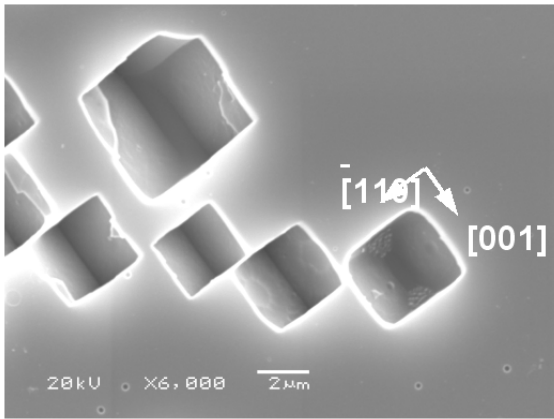


Fig. 7. Pits formed on {110} surface of Al crystal etched at -1.5 V for 100 ms followed by -0.5 V for 100 ms.<sup>2)</sup>

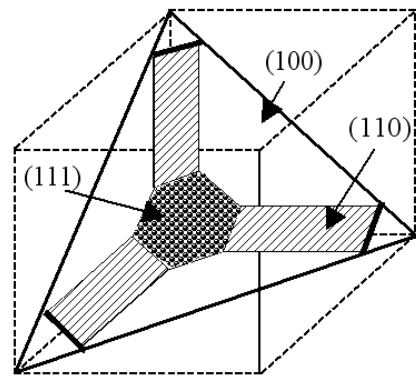
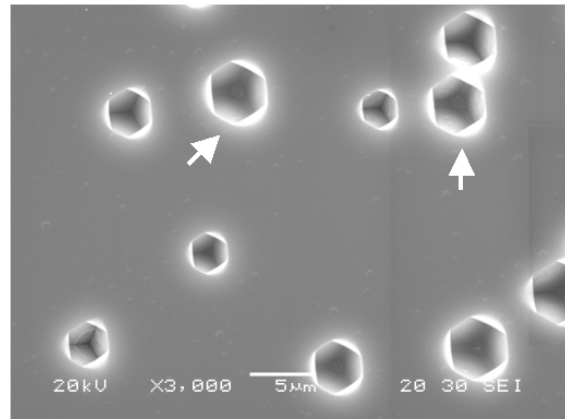


Fig. 8. Pits formed on {111} surface of Al crystal etched at -1.5 V for 100 ms followed by -0.5 V for 100 ms.<sup>2)</sup>

{110}, and {111} planes can be seen, even though the areas of the {110} and {111} planes are much smaller than those of the {100} planes. Since pits on the {100} planes are bounded by the {100} planes, their square shape on the surface is seen and their walls are not clearly seen.

The better delineated shape of the etch pits resulting from ac etching seems to be caused by the formation of more stable passive films possibly due to pH increase during cathodic polarization.

### 3.2 Pit density

Compared with the result of the pulsed dc experiments, the presence of prior cathodic polarization significantly increases the pit density, regardless of the surface orientation (Fig. 9). It can also be seen that the pit density on the {111} surface is higher than those on the {110} and {100} surfaces, while the pit densities on the {110} and {100} surfaces are not very different.

The overall increase in pit density resulting from prior cathodic polarization can be attributed to the cathodic activation process, in which cathodic polarization provides available sites for pit nucleation in the subsequent anodic

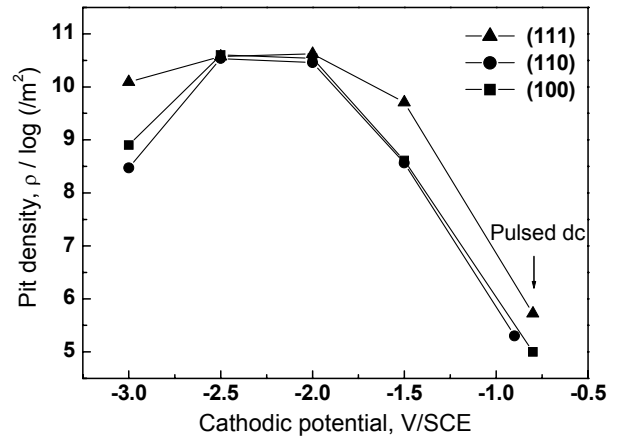


Fig. 9. Measured average values of pit densities for {100}, {110}, and {111} surfaces of aluminum single crystal as a function of prior cathodic potential. Specimens indicated by “Pulsed dc” are maintained at open circuit potential without prior cathodic polarization.<sup>2)</sup>

polarization. The hydrogen reduction reaction causes a deterioration of the passive oxide film on the aluminum. The breakdown of the passive oxide film during cathodic polar-

ization may occur by means of either compositional changes<sup>6,7)</sup> or mechanical rupture of the film.<sup>8,9)</sup>

The blistering of anodic oxide film on aluminum was observed in HCl solution during cathodic polarization.<sup>9)</sup> Although it is rather difficult to find any evidence of blistering of the native oxide film, pits covered by flakes of oxide film are observed after ac etching (Fig. 10). This oxide blistering is considered to occur as a result of the excessive generation of hydrogen atoms at the metal/oxide interfaces, which can be attributed to proton migration caused by the presence of an electric field, which is built up across the oxide film.<sup>10)</sup> Cracking starts at the periphery of the blister, and then the bare aluminum surface itself is exposed to the electrolyte containing the chloride ions. During the subsequent anodic polarization, the bare surface along the periphery of the blister is likely to be attacked.

Although the hydrogen evolution is highest at the cathodic potential of -3 V/SCE, the anodic pitting charges and pit densities are lower than those obtained at the cathodic potential of -2.5 V/SCE. This indicates the existence of an optimum cathodic condition for the maximum pit density to be obtained in the subsequent anodic polarization. At the optimum potential, the minimum pit size is obtained as shown in Fig. 11. The increase in pH near the exposed bare metal surface, caused by the excessive hydrogen evolution at -3 V/SCE, might accelerate the formation of re-passivation film on the bare aluminum surface, thereby limiting the number of sites available for pit nucleation in the subsequent anodic polarization.

### 3.3 Pit growth rate

If the pit current density is independent of time, the average pit current density can be calculated from the total anodic charge and the total active surface area using the following equation:<sup>11)</sup>

$$J_L = Q / \sum St \quad (6)$$

where  $J_L$ ,  $Q$ ,  $S$ , and  $t$  are the average pit current density, the anodic charge, the surface area of an individual pit, and the elapsed time during anodic polarization, respectively. The value of  $S$  for each sample was determined by statistical analysis of more than thirty SEM micrograph frames. However, the above equation was not suitable for the calculation of the pit current density for pits resulting only from anodic polarization, because they had no discrete shape and were unevenly distributed on the surface. For comparison, the pit current density of a polycrystalline aluminum foil etched by pulsed dc waveform was calculated to be 7.5 kA/m<sup>2</sup>.

In order to observe the influence of prior cathodic polar-

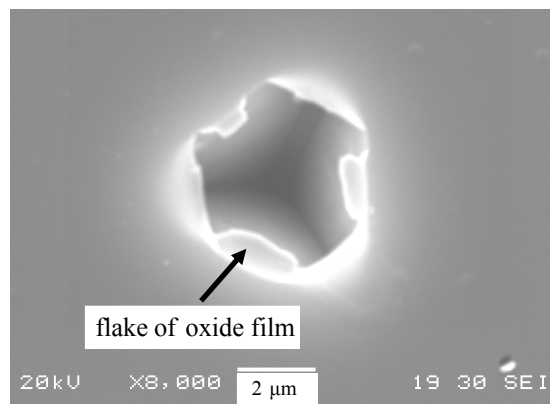


Fig. 10. Pit on (111) single crystal that is partially covered by native oxide film (Etching condition: -1.5 V for 100 ms followed by -0.5 V for 100 ms).<sup>2)</sup>

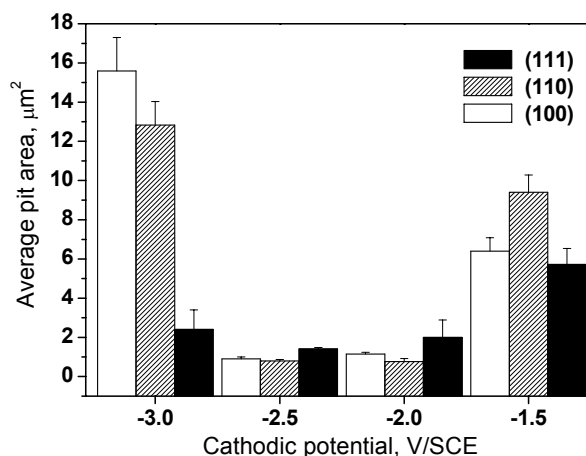


Fig. 11. Measured average values of pit sizes for {100}, {110}, and {111} surfaces of aluminum single crystal as a function of prior cathodic potential.<sup>2)</sup>

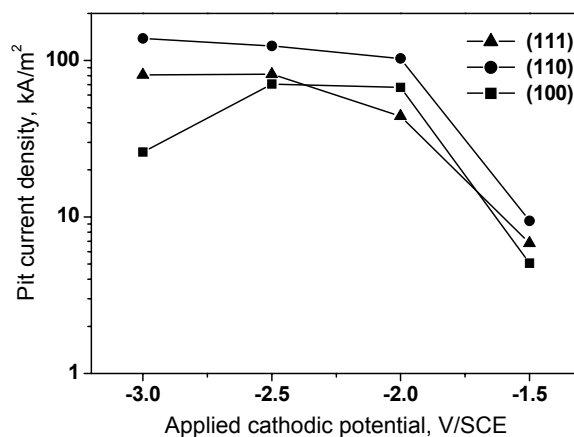
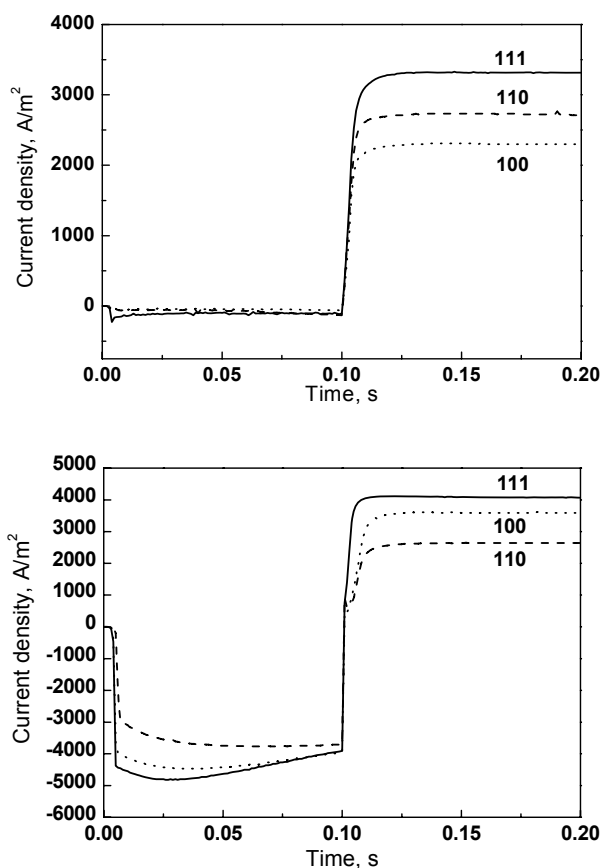


Fig. 12. Calculated values of pit current densities for {100}, {110}, and {111} surfaces of aluminum single crystal as a function of prior cathodic potential.<sup>2)</sup>

ization on pit growth, the pit current density was measured as a function of applied cathodic potential. Since the current density is almost independent of time during anodic polarization, the pit current density is a reflection of pit growth. The pit current density or the pit growth rate generally increases with increasing applied cathodic potential as shown in Fig. 12. It is interesting to note that the {100} surface shows the lowest pit growth rate among the three low index surfaces. This indicates that when the pits grow following nucleation, the {110} and {111} surfaces dissolve faster than the {100} surface.

### 3.4 Potential step experiments

Fig. 13 shows the current-time curves for the {100}, {110}, and {111} surfaces of the aluminum single crystals in the step potential experiments. The initial rise in the anodic current transients is closely related to the rate of pit nucleation and the steady-state current represents the growth of the pits once they are nucleated. At a prior cathodic potential of -2 V/SCE, the initial steep rise in



**Fig. 13.** Transients of current densities for {100}, {110}, and {111} surfaces of aluminum single crystal in step potential experiments in 1 M HCl solutions at 30 °C. (a) cathodic potential -1.5 V, anodic potential -0.5 V and (b) cathodic potential -2 V, anodic potential -0.5 V/ SCE.<sup>2)</sup>

the current indicates that the rate of generation of pits, caused by the breakdown of the passive film, is high. In other words, a large number of pits are nucleated spontaneously. The highest anodic current flow on the {111} surface results in the highest pit density occurring on this surface. It is interesting to note that, at a cathodic potential of -1.5 V/SCE, the steady-state anodic current increases in the order of {100} < {110} < {111}, which is in good agreement with previously reported results, which indicates that the susceptibility to pitting varies in the order of {100} < {110} < {111}.<sup>12)-14)</sup> At a lower potential of -2V/SCE, the susceptibility trend is measured to be a little different, but it seems to be due to a lack of accuracy in the measurements.

Fig. 14 shows cumulative cathodic charges and corresponding anodic charges for the {100}, {110}, and {111} surfaces as a function of cathodic potential in the ac square wave experiments. The cumulative charges were obtained

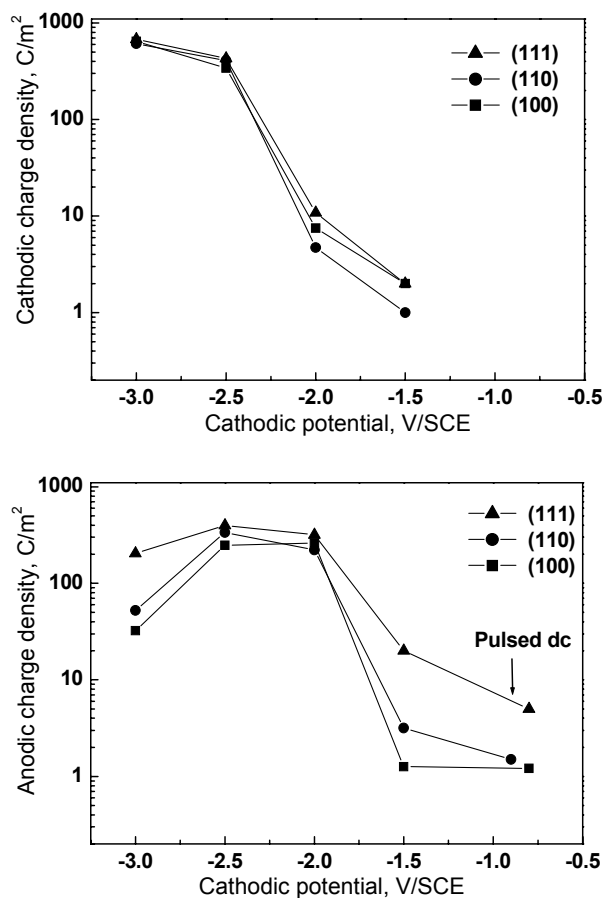


**Fig. 14.** Measured cathodic (a) and anodic (b) charge densities for {100}, {110}, and {111} surfaces of aluminum single crystal as a function of applied cathodic potential in potential step experiments in 1 M HCl solution at 30 °C. Anodic potential was set at -0.5 V/SCE. Charge densities are obtained from integrated area of current density-time curves in Fig. 13.<sup>2)</sup>

by integrating the recorded *i-t* curves in Fig. 13. For comparison, the anodic charges at open circuit potentials measured with pulsed dc are also shown in Fig. 14 (b). It is noted that anodic pitting reactions are greatly enhanced by the presence of cathodic polarization. The anodic pitting reaction increases with increasing prior cathodic potential except at -3 V/SCE. The decrease in cumulative anodic charge at the potential of -3 V/SCE results in a decrease in pit density (Fig. 9) and an increase in pit size (Fig. 11). The cumulative anodic dissolution charge on the {111} surface is always higher than those on the {100} and {110} surfaces.

The mechanism by means of which pit growth occurs is somewhat different from the process of pit initiation. The pit growth is closely related to the amount of exposed metal substrate that is directly in contact with the electrolyte, while the pit nucleation starts with the breakdown of the passive oxide film covering the metal substrate. Thus, both the repassivation and dissolution processes of the exposed metal substrate control the pit growth rate. On the other hand, the stability of the passive film strongly controls the rate of pit initiation.

The observed orientation dependency of the pit nucleation, which generally increases in the order (111) > (110) > (100) but the difference between the {110} and {100} plane is small, is well explained in terms of the stability of the oxide film due to the relative elastic strain energies due to substrate orientations.

#### 4. DC tunnel etching results and discussion

Anodic dissolution of high purity aluminum in hot aqueous chloride solution produces a high density of (m-wide fine tunnels which penetrate the aluminum in the <100> directions at rates of  $\mu\text{m/s}$ . The cross-sectional size of the tunnel is constant or decreases very slowly with increasing depth. The tunnel-etched aluminum foil can serve for electrodes in electrolytic capacitors. According to the results of Herbert *et al.*,<sup>15)</sup> the etch tunnels grow along the <100> directions and the tunnel side walls are made of the {100} planes. They also claimed that the metal surface at the tip of the tunnel appeared to be flat and smooth, indicating that the tip was composed of the {100} planes. Having observed a similar phenomenon, Jackson<sup>16)</sup> suggested that the directional nature of the dissolution appeared to be related to the lower energy required to remove atoms from the {100} planes but gave no detailed reasons to support this idea.

Two ways to sustain the tunnel growth were proposed by Alwitt *et al.*<sup>17)</sup> The first is to have two parallel reactions of tip dissolution and also wall passivation, i.e., dissolution

takes place at the tip of the tunnel, whilst the side walls are passivated. The second is sequential dissolution and passivation. In the second case, a sequence consists of the initiation of a pit at the tunnel tip, pit growth, and passivation of this new surface. A new breakdown takes place on the new surface and the next cycle starts. An important mechanism of the tunnel growth behaviors is passivation, that is to say, a passive oxide film forms on the aluminum during the electrochemical etching, whether the passivation takes place in the tunnel side walls while the tunnel tips actively corrode or the sequential passivation takes place in the tunnel side walls and tunnel tips.

The structure of the passive film formed on the aluminum during the electrochemical etching under high concentrations of chloride solutions at temperatures above 60 °C is not clearly understood yet. However, the results of Dyer and Alwitt<sup>18)</sup> showed that the passive film (the passive film is often called "etch-film") might be a hydroxide, probably in combination with an amorphous oxide. Therefore, the passive film formed on aluminum during the etching is presumed to be similar to that of the hydrous oxide film produced by the reaction of aluminum in hot water. But the thickness of the passive film during the etching is much thinner than that of the hydrous oxide film formed in hot water.

The hydrous oxide is known to be pseudo-boehmite, a poorly crystallized oxyhydroxide which is similar to boehmite ( $\text{AlOOH}$  or  $\text{Al}_2\text{O}_3 \cdot \text{H}_2\text{O}$ ) but contains excess water.<sup>19)-22)</sup> A study by Takahashi *et al.*<sup>23)</sup> indicates that the inner layer of pseudoboehmite adjacent to the aluminum substrate has a very thin compact amorphous structure and the outer layer has a crystalline structure. The average composition and density of pseudoboehmite are  $\text{Al}_2\text{O}_3 \cdot 2.7\text{H}_2\text{O}$  and 2.2-2.4  $\text{g cm}^{-3}$ , respectively.

Jeung *et al.*<sup>1)</sup> carried out DC electroetching of a 100  $\mu\text{m}$ -thick 99.99% aluminum foil with the {100}<001> texture in 1.88 M HCl solution at  $80 \pm 2$  °C. To observe the morphology of the etch tunnels obtained by the electroetching, they made replicas of the tunnels by electrodeposition of copper into the tunnels. Aluminum in the electrodeposited foil was dissolved out in a 1 N NaOH solution, and the copper replica of the etch tunnels was observed under SEM.

Fig. 15 shows the replica of the etch-tunnels, which shows that some tunnels have a square cross section, indicating that the tunnel walls are composed of {100} planes in agreement with earlier results.<sup>15)</sup> However, the tunnels do not have flat fronts as presumed by Herbert and Alkire<sup>15)</sup> and Jackson.<sup>16)</sup> The tunnel tip is rather sharp and appears to consist of the {111} planes. Fig. 15 (c) shows that the cross section of the tunnel is circular rather

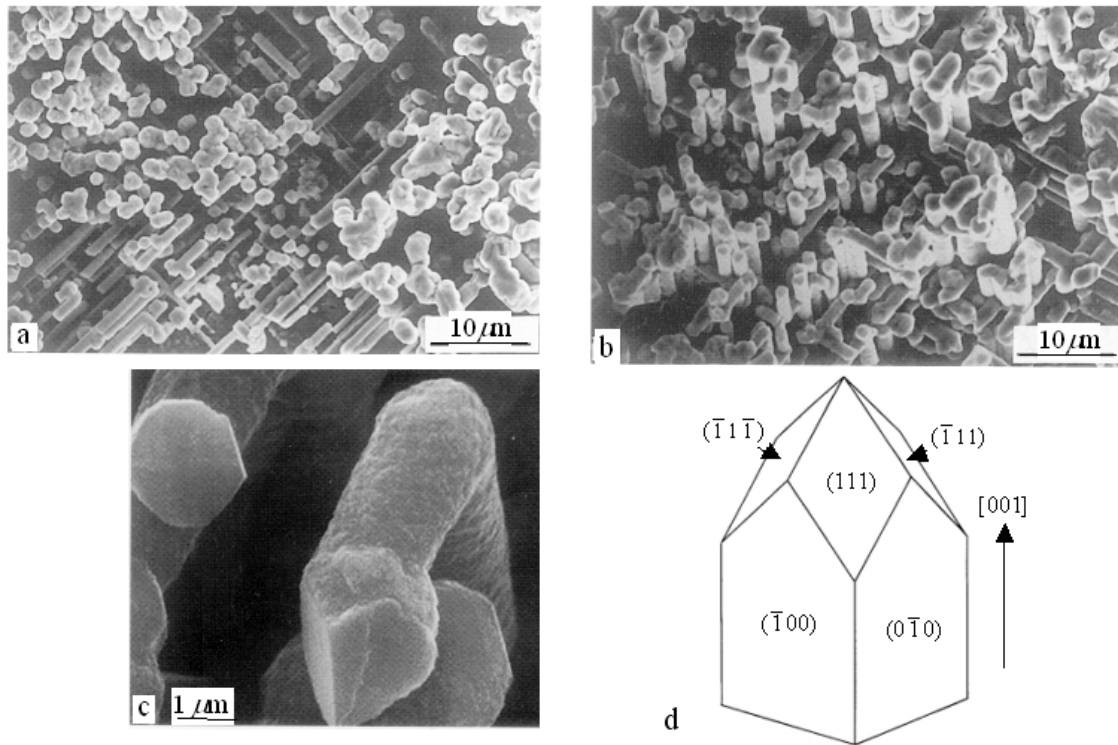


**Fig. 15.** Microstructures of etch tunnels replicated by electrodeposition of copper. (a) Top view, (b) skewed view, (c) tunnel tips composed of  $\{111\}$  planes, (d) model of tunnel tip.<sup>1)</sup>

than square. Higher temperatures tend to make circular tunnels. Occasionally it can be seen that the diameter of the front region of the tunnels is slightly larger than that of the back part. This indicates that the passive oxide film has formed on the wall, while dissolution takes place at the tip. From Fig. 15 (c), the passive oxide film is estimated to be about  $0.1 \mu\text{m}$  thick. This result is compatible with the tip dissolution and wall passivation model rather than the sequential dissolution and passivation to sustain tunnel growth.

The stability of the passive film on the wall depends on crystal planes of the aluminum substrate, as discussed before. The films on the  $\{100\}$  planes are the most stable and least attacked. Therefore, the tunnel walls consist of the  $\{100\}$  planes. Meanwhile, the tunnel tip, where active corrosion takes place, would tend to be made of four closely packed  $\{111\}$  planes in order to minimize the surface energy. These situations are depicted in Fig. 15 (d), which gives rise to the  $\langle 100 \rangle$  tunnel etching.

Fig. 15 also shows two mutually perpendicular tunnels normal to the thickness direction. Let the thickness direction be the  $[001]$  direction, then the two mutually perpendicular directions must be the  $[100]$  and the  $[101]$  directions. According to the tip-dissolution and wall-passivation model, as the etch tunnel grows, the etch-film grow

behind the tunnel tip, resulting in an increase in film stress. When the peak-stress in the film reaches its fracture stress, the film is cracked. This situation is equivalent to the schematic illustration in Fig. 3. New etching can start at the crack and grow in the  $\langle 100 \rangle$  directions normal to the primary etch tunnel. This seems to be the case of tunneling in Fig. 15.

In summary, the  $\langle 100 \rangle$  tunnel etching of aluminum when subjected to DC electroetching in HCl solution is attributed to the fact that the tunnel tip region, where the active corrosion reaction takes place, tends to be made of  $\{111\}$  planes in order to minimize the surface energy, whilst the subsequent tunnel wall is made up of the  $\{100\}$  planes, because the passive oxide film forms on the planes, along which the biaxial elastic modulus is smallest and therefore would be least attacked. As the etch tunnel grows, the etch-film grow behind the tunnel tip, resulting in an increase in film stress. When the peak-stress in the film reaches its fracture stress, the film is cracked. New etching can start at the crack and grow in the  $\langle 100 \rangle$  directions normal to the primary etch tunnel.

## 5. Conclusions

The morphology, number density, growth rate, current

density, and cathodic and anodic charge densities of etch pits are dependent on orientations of aluminum. Most etch pits are bounded by the {100} planes, on which the re-passivated film is the most stable. Occasionally etch pits bounded by the {100}, {110}, and {111} planes can be seen, even though the areas of the {110} and {111} planes are much smaller than those of the {100} planes.

The pit density on the {111} surface is higher than those on the {110} and {100} surfaces, while the pit densities on the {110} and {100} surfaces are not very different. The increased pit density on aluminum in the presence of prior cathodic polarization can be attributed to an increase in the number of nucleation sites, resulting from the breakdown of the oxide film during the cathodic polarization.

The {100} surface shows the lowest pit growth rate among the {100}, {110}, and {111} surfaces, indicating that when the pits grow following nucleation, the {110} and {111} surfaces dissolve faster than the {100} surface. At a cathodic potential of -1.5 V/SCE, the steady-state anodic current increases in the order of {100} < {110} < {111} surface, which indicates that the susceptibility to pitting varies in the order of {100} < {110} < {111} surface.

The above behavior is associated with the stability or the strain energy of the aluminum oxide film, which is dependent on the orientation of the underlying aluminum. The stability increases with decreasing strain energy. The oxide films on the {100} surfaces of aluminum are the most stable, and those on the film on the {111} surfaces are the least stable.

The <100> tunnel etching of aluminum when subjected to DC electroetching in HCl solution is attributed to the fact that the tunnel tip region, where the active corrosion reaction takes place, tends to be made of {111} planes in order to minimize the surface energy, whilst the subsequent tunnel wall is made up of {100} planes, because the passive oxide film is formed on the plane, along which the biaxial elastic modulus is smallest and therefore would be least attacked. As the etch tunnel grows, the etch-film grow behind the tunnel tip, resulting in an increase in film stress. When the peak-stress in the film reaches its fracture

stress, the film is cracked. New etching can start at the crack and grow in the <100> directions normal to the primary etch tunnel.

## References

1. J.-H. Jeong, C.-H. Choi, and D. N. Lee, *J. Mater. Sci.*, **31**, 5811 (1996).
2. J. H. Seo, J.-H. Ryu, and D. N. Lee, *J. Electrochem. Soc.*, **150**, B433 (2003).
3. D. N. Lee, *Mater. Sci. Forum*, **408** 75 (2002).
4. P. M. Sutton, *Phys. Rev.*, **91**, 816 (1953).
5. D. N. Lee, *Thin Solid Films*, **434**, 183 (2003).
6. C.-F. Lin and K. R. Hebert, *J. Electrochem. Soc.*, **137**, 3723 (1990).
7. C.-F. Lin and K. R. Hebert, *J. Electrochem. Soc.*, **141**, 104 (1994).
8. H. Takahashi, K. Hujiwara, and M. Seo, *Corros. Sci.*, **36**, 689 (1994).
9. J. H. Seo and D. N. Lee, *Corros. Sci. Tech.*, **31**, 291 (2002).
10. J. H. Seo and D. N. Lee, *J. Electrochem. Soc.*, **150**, B329 (2003).
11. J. Tousek, *Localized Corrosion of Metals*, Trans Tech Publications, Switzerland (1985).
12. M. Yasuda, F. Weinberg, and D. Tromans, *J. Electrochem. Soc.*, **137**, 3708 (1990).
13. K. Fukuoka and N. Ohsawa, *Sumitomo Light Metal Technical Reports*, **35**, 90 (1994).
14. G. M. Treacy and C. B. Breslin, *Electrochim. Acta*, **43**, 1715 (1998).
15. K. R. Hebert and R. C. Alkire, *J. Electrochem. Soc.*, **135**, 2447 (1988).
16. N. F. Jackson, *Electrocomponent Sci. technology*, **2**, 33 (1975).
17. R. S. Alwitt, H. Uchi, T. R. Beck, and R. C. Alkire, *J. Electrochem. Soc.*, **138**, 13 (1984).
18. C. K. Dyer and R. S. Alwitt, *J. Electrochem. Soc.*, **128**, 300 (1981).
19. R. S. Alwitt, *J. Electrochem. Soc.*, **118**, 1730 (1971).
20. R. K. Hart, *Proc. Roy. Soc. London. Ser., A* **236**, 68 (1956).
21. R. K. Hart, *Trims Faraday Soc.*, **53**, 1020 (1957).
22. W. Vedder and D. A. Vermile, *Electrochim Acta*, **65**, 567 (1969).
23. H. Takahashi, Y. L'mehara, and T. Miyamamoto, *J. Surf. Fin. Jpn.*, **38**, 67 (1987).